HEAVY FLAVOUR RESULTS FROM ATLAS*

Andreas Warburton

on behalf of the ATLAS Collaboration

McGill University, Montréal, Canada

Received 31 March 2025, accepted 22 April 2025, published online 26 June 2025

Heavy flavour production cross sections and lifetimes in hadron colliders inform and challenge perturbative and non-perturbative quantum chromodynamics (QCD) determinations, while providing sensitivity to physics beyond the Standard Model. Using up to 140 fb^{-1} of pp collisions at $\sqrt{s} = 13$ TeV from Run 2 of the LHC, recent results from the ATLAS experiment are presented: differential charmonium production cross sections extending up to transverse momenta (p_{T}) of 360 GeV (J/ψ) and 140 GeV ($\psi(2S)$), differential open-charm $D^{\pm}$ and $D_s^{\pm}$ meson production cross sections extending up to $p_{\mathrm{T}} = 100$ GeV, and the open-beauty B^0 meson effective lifetime of $\tau_{B^0} = 1.5053 \pm 0.0012(\mathrm{stat.}) \pm 0.0035(\mathrm{syst.})$ ps, to date the most precise single measurement of this quantity.

DOI:10.5506/APhysPolBSupp.18.5-A35

1. Introduction

ATLAS heavy-flavour physics studies span numerous subjects, including the production cross sections of heavy onia and open-flavour hadrons; decay branching fractions, CP studies, and lifetimes; and the spectroscopy of exotic and conventional hadrons [1]. The topics presented constitute the latest results extending two-, three-, and four-track heavy-meson reconstructions in the challenging hadron-collision environment, first encountered at the Fermilab Tevatron [2, 3]. Relevant strengths of the ATLAS detector [4] include modes with final-state muons and decay vertexing, as well as extended access to previously uncharted kinematic ranges. Extensive muon-spectrometer and inner-detector tracking systems [4], and in particular a multi-level trigger system capable of di-muon and single-muon transverse-momentum (p_{T}) thresholds of 4, 6, and 11 GeV [5], enable such competitive heavy-flavour measurements. The following new ATLAS results are obtained in pp collisions at $\sqrt{s} = 13$ TeV from up to an integrated luminosity of 140 fb^{-1} acquired during Run 2 of the Large Hadron Collider (LHC).

* Presented at the 31st Cracow Epiphany Conference on the *Recent LHC Results*, Kraków, Poland, 13–17 January, 2025.

2. Charmonium: differential J/ψ and $\psi(2S)$ meson cross sections

Heavy-quarkonium systems provide unique probes near the boundary between perturbative and non-perturbative quantum chromodynamics (QCD). While $c\bar{c}$ mesons have been studied for several decades, significant theoretical and experimental challenges remain. Charmonium states at the LHC arise either via prompt short-lived QCD processes in pp interactions or feed-down from heavier states, or in non-prompt decays of beauty hadrons. To date, theoretical perturbative QCD calculations describe non-prompt $c\bar{c}$ meson production better than prompt production.

Prior to this ATLAS study, measured kinematic ranges of charmonium production extended up to transverse momenta of $p_{\mathrm{T}} = 100$ GeV. In this work, we present new J/ψ cross-section results with $p_{\mathrm{T}} < 360$ GeV and $\psi(2S)$ results with $p_{\mathrm{T}} < 140$ GeV. This is accomplished with an updated trigger strategy to overcome insufficient angular resolution at high p_{T} by requiring conventional di-muon triggers for $p_{\mathrm{T}}(\psi) < 60$ GeV and single-muon triggers, with a 50 GeV muon p_{T} threshold, for $p_{\mathrm{T}}(\psi) > 60$ GeV. Two-dimensional fits in di-muon mass $m_{\mu\mu}$ and pseudo-proper decay time τ distinguish between J/ψ and $\psi(2S)$ states and prompt and non-prompt production. Figure 1 shows projections of the invariant mass distribution and the pseudo-proper decay time $\tau = m_{\mu\mu} L_{xy}/p_{\mathrm{T}}$, where L_{xy} is the transverse distance between the primary and the di-muon vertex, projected onto the p_{T} direction of the di-muon system.

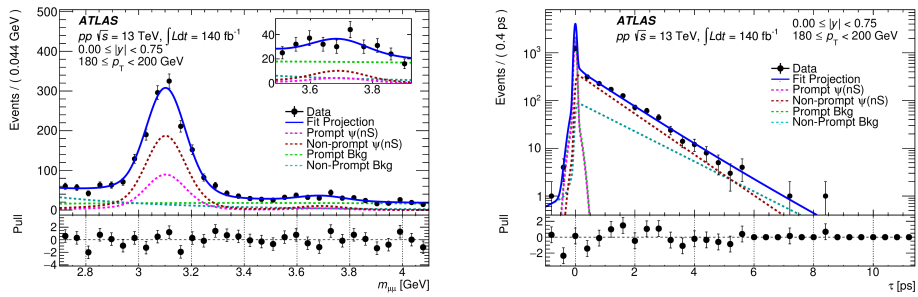

Fig. 1. Di-muon invariant mass [left] and pseudo-proper decay time [right] projections of the fit result in the central $0.00 \leq |y| < 0.75$ rapidity and high-transverse-momentum $180 \leq p_{\mathrm{T}} < 200$ GeV bins [6].

The 2D fit, performed in 3 rapidity (y) and 34 p_{T} bins (spanning 8–360 GeV), for a total of 102 phase-space bins and assuming a nominal isotropic spin-alignment scenario, provides differential J/ψ ($\psi(2S)$) production cross sections spanning 9 (6) orders of magnitude, as shown in Fig. 2 for the prompt cases. Figure 3 shows the corresponding non-prompt production fractions, which rise at lower p_{T} and reach a plateau at higher p_{T}.

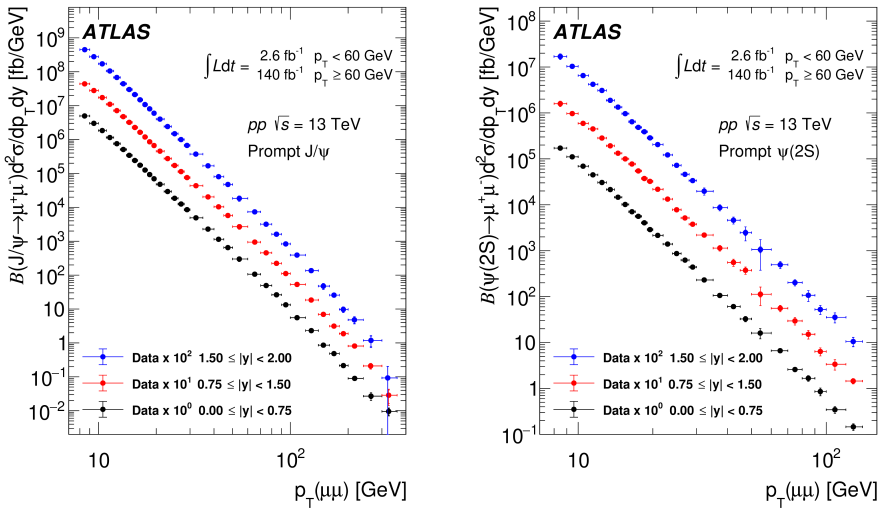

Fig. 2. Differential cross sections for prompt J/ψ [left] and $\psi(2S)$ [right] meson production [6]. For clarity, scaling factors of 1, 10, or 100 are applied to the rapidity regions of $0.00 \leq |y| < 0.75$, $0.75 \leq |y| < 1.5$, and $1.5 \leq |y| < 2.0$, respectively.

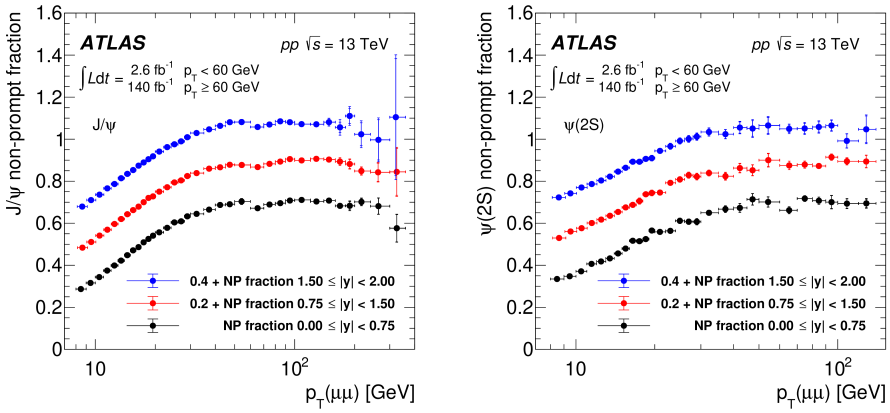

Fig. 3. Non-prompt production fraction of J/ψ [left] and $\psi(2S)$ [right] mesons [6]. For clarity, vertical shifts of 0, 0.2, or 0.4 are applied to the rapidity regions of $0.00 \leq |y| < 0.75$, $0.75 \leq |y| < 1.5$, and $1.5 \leq |y| < 2.0$, respectively.

The ATLAS results, which show consistency with other LHC experiments at lower transverse momenta (see Fig. 4), are compared with various theoretical predictions (listed in Ref. [6]) in Fig. 5 for the J/ψ case. In the case of prompt J/ψ production, the predicted spectra are harder than those measured, and there is room for the models to improve. The non-prompt predictions show better agreement, though still overestimate the cross sections at higher p_{T}. Similar trends are found for the $\psi(2S)$ analogues [6].

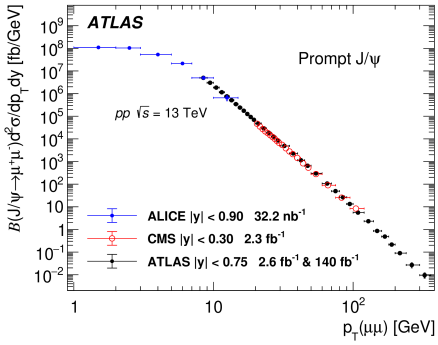

Fig. 4. Comparison of the differential cross section of prompt J/ψ production measured by ATLAS [6] in the central rapidity range with the CMS [7] and ALICE [8] results in the closest-matching rapidity ranges.

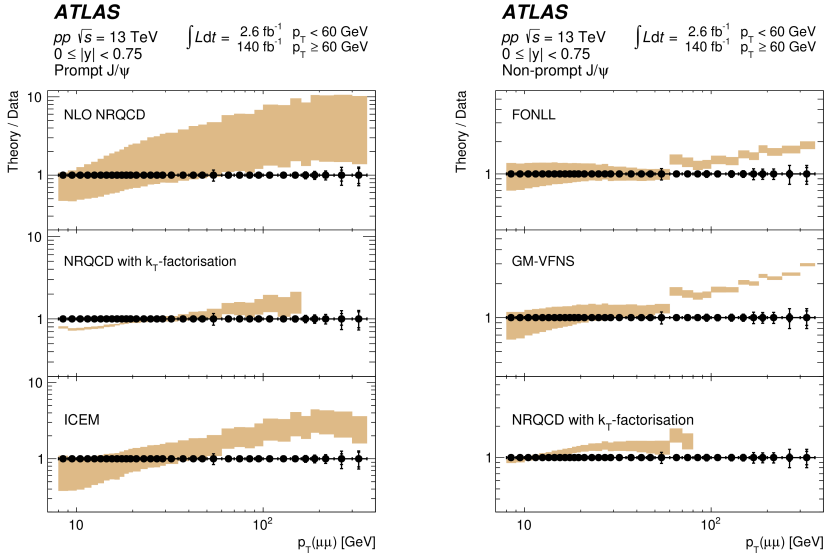

Fig. 5. Ratios of theoretical predictions, mentioned in Ref. [6], to the data measurements for the prompt [left] and non-prompt [right] production of a J/ψ meson in the central rapidity region [6].

3. Open charm: differential $D^{\pm}$ and $D_s^{\pm}$ meson cross sections

Heavy-hadron production in pp collisions fundamentally tests perturbative QCD calculations, which have sizeable uncertainties due to coping with hard-scatter energy scales comparable to the heavy-quark masses, modelling non-perturbative effects such as hadronisation, and describing prompt and non-prompt production [9]. In this ATLAS study, $D^{\pm}$ and $D_s^{\pm}$ production cross sections are measured, for the first time out to $p_{\mathrm{T}} = 100$ GeV, simulta-

neously and differentially using the $D^{\pm}_{(s)} \to \phi\pi^{\pm} \to \mu^{+}\mu^{-}\pi^{\pm}$ channels: less abundant than the analogous $\phi \to K^{+}K^{-}$ process, but encountering less background and enabling exploitation of di-muon triggers.

Di-muons selected by the triggers are required to have an opposite charge and satisfy invariant-mass criteria. The three-track candidates are subjected to total-charge, minimum p_{T}, and secondary-vertex criteria. The main observable is the three-track invariant mass $m_{\mu\mu\pi}$, indicated in Fig. 6. Signal $m_{\mu\mu\pi}$ yields are extracted using an extended unbinned maximum likelihood fit designed to be compatible with data in a broad set of kinematic regions while using a small number of parameters: Voigtian (Breit–Wigner convolved with Gaussian) signal probability density functions (PDFs), a Gaussian-constrained $m_{D_s^{\pm}} - m_{D^{\pm}}$ world-average mass difference [10], and an exponential background component.

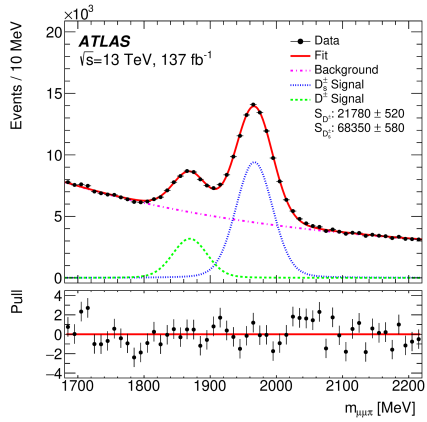

Fig. 6. Invariant mass distribution of the di-muon–plus–track candidates [9]. The unbinned fit is shown as a solid line, with the signal components for the $D^{\pm}$ and $D_s^{\pm}$ resonance fit presented as dashed and dotted lines, respectively; the background-only contribution is shown as a dash-dotted line.

Prompt ($pp \to c\bar{c}X \to D^{\pm}_{(s)}X'$) and non-prompt ($pp \to b\bar{b}Y \to cY' \to D^{\pm}_{(s)}Y''$) production processes manifest differently in the ATLAS detector, so their relative contributions are constrained using the pseudo-proper decay time observable computed at the three-track vertex and depicted in Fig. 7. The lifetime fits are performed using convolutions of Gaussian and error functions with one (two) exponentials for prompt (non-prompt) PDFs.

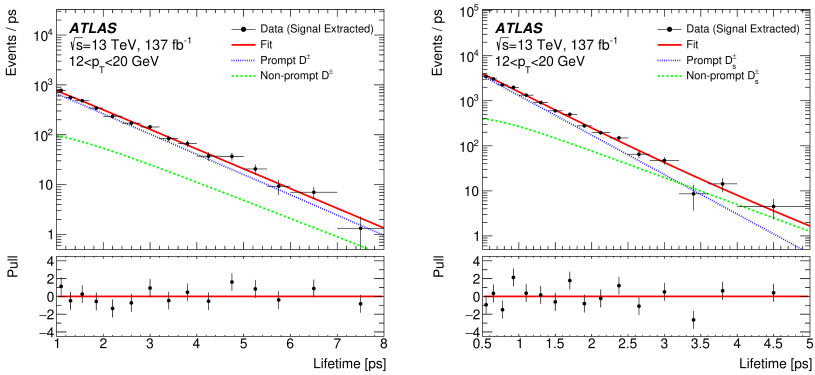

Fig. 7. Template fits to the lifetime distribution extracted from data for $D^{\pm}$ [left] and $D_s^{\pm}$ [right] mesons in the range of $12 < p_{\mathrm{T}} < 20$ GeV [9].

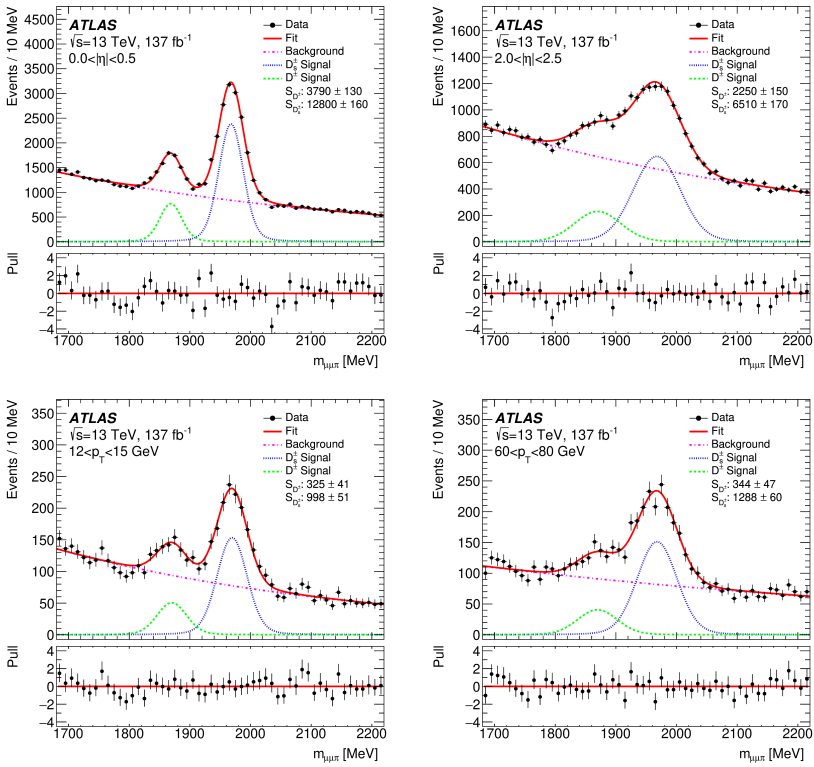

Fig. 8. Examples of fits to the invariant-mass distributions $m_{\mu\mu\pi}$ in regions of central rapidity [top left], forward rapidity [top right], lower transverse momentum [bottom left], and higher transverse momentum [bottom right] [9].

Cross sections are determined in nine p_{T} bins in the 12–100 GeV range and five pseudorapidity bins in the $|\eta| < 2.5$ range by extracting signal yields from invariant mass fits (see Fig. 8 for some examples) for $D^{\pm}$ and $D_s^{\pm}$ candidates simultaneously. Corrections for reconstruction efficiencies are applied in each bin, suitably weighted for prompt and non-prompt production fractions determined from the lifetime fits shown in Fig. 7. Also accounted for are the appropriate branching-fraction [10] products, with $\mathcal{B}(D^{\pm} \to \phi(\mu\mu)\pi^{\pm}) = \mathcal{B}(D^{\pm} \to \phi\pi^{\pm}) \times \mathcal{B}(\phi \to \mu^{+}\mu^{-})$ in the $D^{\pm}$ meson case. In the $D_s^{\pm}$ meson case, a select quotient of world-average branching fractions is used since its uncertainty is less than that of the $\mathcal{B}(D_s^{\pm} \to \phi\pi^{\pm})$ world average [10]: $\mathcal{B}(D_s^{\pm} \to \phi(\mu\mu)\pi^{\pm}) = \frac{\mathcal{B}(D_s^{\pm} \to \phi(K^{+}K^{-})\pi^{\pm})}{\mathcal{B}(\phi \to K^{+}K^{-})} \times \mathcal{B}(\phi \to \mu^{+}\mu^{-})$.

The resulting $D^{\pm}$ and $D_s^{\pm}$ meson production cross sections [9], differential in either $|\eta|$ or p_{T}, are given in Fig. 9 and compared with theoretical GM-VFNS and FONLL [9] predictions. For $D^{\pm}$ meson production, at low p_{T} and in all $|\eta|$ bins, both the GM-VFNS and FONLL predictions indicate

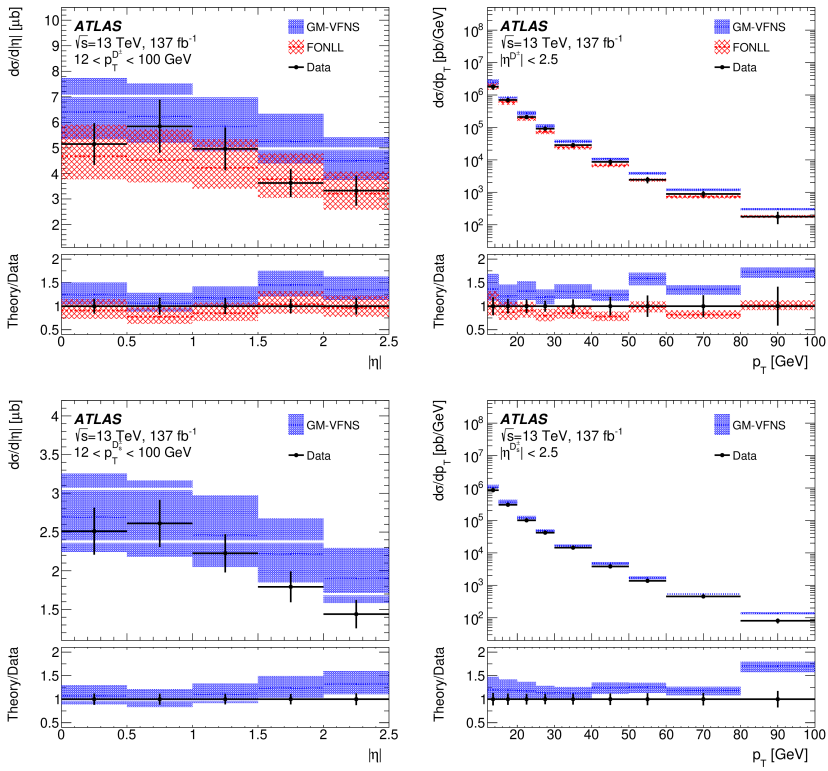

Fig. 9. Differential cross sections for $D^{\pm}$ mesons in bins of $|\eta|$ [top left] and p_{T} [top right], and for $D_s^{\pm}$ mesons in bins of $|\eta|$ [bottom left] and p_{T} [bottom right] [9].

good agreement, with GM-VFNS showing some overestimation at high p_{T}. For $D_s^{\pm}$ production, only GM-VFNS predictions are available for comparison; these exhibit a similar upward deviation at higher p_{T} values.

4. Open beauty: precision B^0 meson lifetime measurement

Precise B-meson lifetimes and their ratios test weak-interaction roles and have potential sensitivity to physics beyond the Standard Model. In this study, weak hadronic spectator-internal colour-suppressed $B^0 \to J/\psi K^{*0}$ decays are reconstructed and their effective lifetime τ_{B^0} is extracted. Candidates are reconstructed by identifying a vertex shared by the triggered di-muons and two charged tracks. For each B^0 candidate, a pseudo-proper decay time is defined by the four-track vertex. A two-dimensional unbinned maximum likelihood fit simultaneously examines both the invariant mass and pseudo-proper decay time quantities; projections are depicted in Fig. 10.

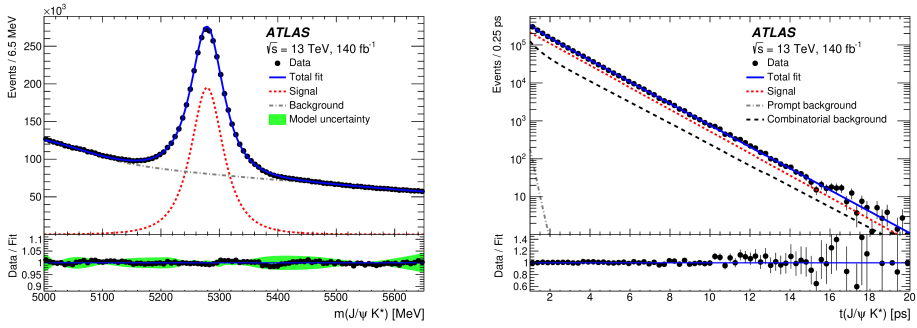

Fig. 10. Invariant mass [left] and pseudo-proper decay time [right] fit projections for the $B^0 \to J/\psi K^{*0}$ sample [11] shown in the pseudo-proper decay time range $t \in (1; 20)$ ps.

The measured effective B^0-meson lifetime is determined [11] to be $\tau_{B^0} = 1.5053 \pm 0.0012(\mathrm{stat.}) \pm 0.0035(\mathrm{syst.})$ ps. Figure 11 outlines some consistency and stability testing of this result compared to three sub-sample data-taking periods. Using parameters from external sources [11], the average decay width is found to be $\Gamma_d = 0.6639 \pm 0.0005(\mathrm{stat.}) \pm 0.0016(\mathrm{syst.}) \pm 0.0038(\mathrm{ext.})$ ps^{-1}, where the uncertainties are statistical, systematic, and from external sources. Using the earlier ATLAS measurement [12] of Γ_s in $B_s^0 \to J/\psi\phi$ decays, a value for the ratio of the average decay widths Γ_d and Γ_s for B^0 and B_s^0 mesons, respectively, is also derived to be $\frac{\Gamma_d}{\Gamma_s} = 0.9905 \pm 0.0022(\mathrm{stat.}) \pm 0.0036(\mathrm{syst.}) \pm 0.0057(\mathrm{ext.})$.

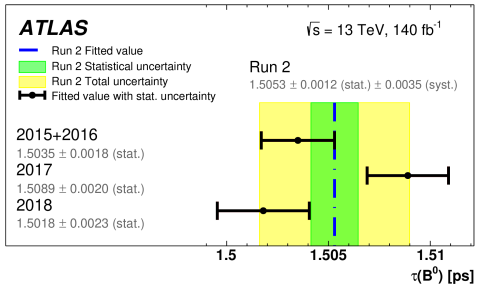

Fig. 11. Fitted values of the effective B^0 lifetime, measured with $B^0 \to J/\psi K^{*0}$ decays, for the 2015+2016, 2017, and 2018 subsamples compared to the value for the entire sample [11].

Figure 12 compares the new ATLAS result for the effective B^0-meson lifetime with recent measurements by ATLAS and several other experiments [11, 13–21], finding compatibility with most. The world-average value [10] of 1.517 ± 0.004 ps, which draws on the full history of B^0 lifetime measurements, differs by 2.1σ.

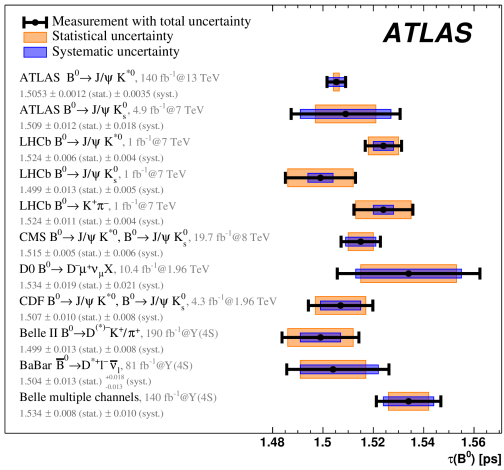

Fig. 12. A comparison of the current ATLAS result [11] for the effective B^0-meson lifetime with the previous ATLAS result [13] in the $B^0 \to J/\psi K^0_S$ channel, and with those from other measurements [14–21].

5. Conclusions

The ATLAS heavy-flavour physics programme is amassing competitive results from Run 2 of the LHC operations. Differential two-track charmonium production cross sections have been extended up to $p_T = 360$ GeV

(J/ψ) and 140 GeV ($\psi(2S)$), constituting the most comprehensive measurement of charmonium production to date. New differential three-track $D^{\pm}$- and $D_s^{\pm}$-meson production cross sections have now been extended up to $p_{\mathrm{T}} = 100$ GeV, for the first time in the case of the $D_s^{\pm}$ state. Both the charmonium and open-charm measurements reveal limitations in the consulted theory predictions, especially at higher ranges in p_{T}. Finally, the first four-track precision B^0-meson effective lifetime measurement in pp collisions at 13 TeV is found to be compatible with most other recent results and is now the most precise single measurement. Further ATLAS heavy-flavour results are under preparation, including combinations of Run 2 and Run 3 data samples [1].

REFERENCES

[1] ATLAS Collaboration, https://twiki.cern.ch/twiki/bin/view/AtlasPublic/BPhysPublicResults
[2] CDF Collaboration (F. Abe *et al.*), *Phys. Rev. D* **58**, 072001 (1998).
[3] A. Warburton, arXiv:hep-ex/0108046.
[4] ATLAS Collaboration (G. Aad *et al.*), *J. Instrum.* **3**, S08003 (2008).
[5] ATLAS Collaboration (G. Aad *et al.*), *J. Instrum.* **15**, P09015 (2020).
[6] ATLAS Collaboration (G. Aad *et al.*), *Eur. Phys. J. C* **84**, 169 (2024).
[7] CMS Collaboration (A.M. Sirunyan *et al.*), *Phys. Lett. B* **780**, 251 (2018).
[8] ALICE Collaboration (S. Acharya *et al.*), *J. High Energy Phys.* **2022**, 190 (2022).
[9] ATLAS Collaboration, arXiv:2412.15742 [hep-ex].
[10] Particle Data Group (S. Navas *et al.*), *Phys. Rev. D* **110**, 030001 (2024).
[11] ATLAS Collaboration, arXiv:2411.09962 [hep-ex], accepted for publication in *Eur. Phys. J. C*.
[12] ATLAS Collaboration (G. Aad *et al.*), *Eur. Phys. J. C* **81**, 342 (2021).
[13] ATLAS Collaboration (G. Aad *et al.*), *Phys. Rev. D* **87**, 032002 (2013).
[14] LHCb Collaboration (R. Aaij *et al.*), *J. High Energy Phys.* **2014**, 114 (2014).
[15] LHCb Collaboration (R. Aaij *et al.*), *Phys. Lett. B* **736**, 446 (2014).
[16] CMS Collaboration (A.M. Sirunyan *et al.*), *Eur. Phys. J. C* **78**, 457 (2018).
[17] D0 Collaboration (V.M. Abazov *et al.*), *Phys. Rev. Lett.* **114**, 062001 (2015).
[18] CDF Collaboration (T. Aaltonen *et al.*), *Phys. Rev. Lett.* **106**, 121804 (2011).
[19] Belle II Collaboration (F. Abudinén *et al.*), *Phys. Rev. D* **107**, L091102 (2023).
[20] BaBar Collaboration (B. Aubert *et al.*), *Phys. Rev. D* **73**, 012004 (2006).
[21] Belle Collaboration (K. Abe *et al.*), *Phys. Rev. D* **71**, 072003 (2005); *Erratum ibid.* **71**, 079903 (2005).